

Comparison of mid-velocity fragment formation with projectile-like decay

S. Hudan, R. Alfaro, B. Davin, Y. Larochele, H. Xu,^{*} L. Beaulieu,[†] T. Lefort,[‡] R. Yanez,[§] and R.T. de Souza
*Department of Chemistry and Indiana University Cyclotron Facility
Indiana University, Bloomington, IN 47405*

R.J. Charity and L.G. Sobotka
Department of Chemistry, Washington University, St. Louis, MO 63130

T.X. Liu, X.D. Liu, W.G. Lynch, R. Shomin, W.P. Tan, M.B. Tsang, A. Vander Molen, A. Wagner,[¶] and H.F. Xi
*National Superconducting Cyclotron Laboratory and Department of Physics and Astronomy
Michigan State University, East Lansing, MI 48824*

(Dated: July 10, 2018)

The characteristics of intermediate mass fragments (IMFs: $3 \leq Z \leq 20$) produced in mid-peripheral and central collisions are compared. We compare IMFs detected at mid-velocity with those evaporated from the excited projectile-like fragment (PLF*). On average, the IMFs produced at mid-velocity are larger in atomic number, exhibit broader transverse velocity distributions, and are more neutron-rich as compared to IMFs evaporated from the PLF*. In contrast, comparison of mid-velocity fragments associated with mid-peripheral and central collisions reveals that their characteristics are remarkably similar despite the difference in impact parameter. The characteristics of mid-velocity fragments are consistent with low-density formation of the fragments. Neutron deficient isotopes of even Z elements manifest higher kinetic energies than heavier isotopes of the same element for both PLF* and mid-velocity emission. This result may be due to the decay of long-lived excited states in the field of the emitting system.

PACS numbers: PACS number(s): 25.70.Mn

I. INTRODUCTION

Cluster emission from nuclear matter can arise from a wide range of phenomena, such as statistical evaporation from normal density nuclear matter at modest excitation [1] or the multi-fragmentation of low-density nuclear matter at high excitation induced by GeV hadronic projectiles [2]. Collision of two heavy-ions at intermediate energies ($25 \text{ MeV} \leq E/A \leq 100 \text{ MeV}$) also results in copious intermediate mass fragment (IMF : $3 \leq Z \leq 20$) production [3, 4]. Considerable attention has been focused on understanding the conditions governing the maximum fragment yield [5, 6] and the characteristics of the fragments produced [7, 8]. In peripheral collisions of two intermediate-energy ($20 \leq E/A \leq 100 \text{ MeV}$) heavy nuclei ($A \sim 100$) a dissipative binary collision occurs resulting in the formation of an excited projectile-like fragment (PLF*) and target-like fragment (TLF*). The dominant IMF yield in such collisions is observed at velocities intermediate between the de-excited PLF* and TLF*, and is not-attributable to the standard statistical decay of ei-

ther of the two reaction partners [9, 10]. The IMFs in this kinematical region are referred to as mid-velocity IMFs. For more central collisions, the distinctive binary nature of the collision is no longer apparent, nevertheless most of the IMF emission occurs in the same kinematical region as in more peripheral collisions. While for more peripheral collisions, the dynamical nature of mid-velocity fragments has been shown [11, 12, 13, 14], in the case of central collisions, statistical approaches are generally used to understand the fragment production [15, 16, 17].

On general grounds, the size, composition, and kinetic energies of the observed clusters, apart from their yield, can be related to the composition and excitation of the disintegrating system. For example, the composition of fragments, namely their neutron-to-proton ratio, may provide information on the N/Z of the disintegrating system [18, 19]. Several experiments have established the neutron enrichment of IMFs and light clusters ($Z \leq 2$) at mid-velocity [15, 16, 20, 21]. The observation of neutron-rich fragments in this kinematic region has been interpreted as the N/Z fractionation of hot nuclear material into a neutron-rich gas and a proton-rich liquid [15]. As with any claim of “enrichment” of a quantity, it is necessary to establish the appropriate reference with respect to which the enrichment occurs. We propose that the most appropriate reference for investigating possible enrichment of mid-rapidity fragments is the N/Z of the emitted fragments from near normal density nuclear matter.

In this work, we examine the fragment characteristics largely independent of the probability of their formation.

^{*}Present address: Institute of Modern Physics, CAS, Lanzhou, China.

[†]Present address: Université Laval, Quebec, Canada.

[‡]Present address: Université de Caen, Caen, France.

[§]Present address: Department of Nuclear Physics, The Australian National University, Canberra, Australia.

[¶]Present address: Institute of Nuclear and Hadron Physics, Dresden, Germany.

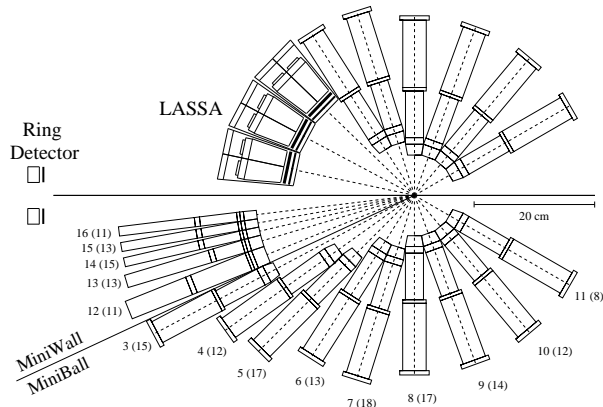


FIG. 1: Experimental setup used to study the reaction $^{114}\text{Cd}+^{92}\text{Mo}$ at $E/A=50$ MeV. The number of detectors in each azimuthal ring of the Miniball/Miniwall array is indicated in parentheses.

We show that, at mid-velocity, the fragment characteristics manifest significant differences as compared to those evaporated from near normal density nuclear matter. In contrast, similar fragment characteristics at mid-velocity are observed both for mid-peripheral collisions and central collisions. In contrast to previous results [16], the size of the emitting system is shown to *not* be the determining factor in the composition of the emitted fragments.

To investigate the factors influencing fragment composition, we measured IMF and light-charged-particle (LCP: $1 \leq Z \leq 2$) emission in the reaction $^{114}\text{Cd} + ^{92}\text{Mo}$ at $E/A=50$ MeV. We examine mid-peripheral collisions in which the survival of a well defined projectile-like fragment occurs. Emission from the PLF* (which presumably is at near normal density) provides a suitable reference for understanding mid-velocity IMF emission in the same collisions. We subsequently compare mid-velocity IMFs associated with mid-peripheral collisions and those associated with central collisions.

II. EXPERIMENTAL SETUP

Charged-particles produced in the reaction $^{114}\text{Cd}+^{92}\text{Mo}$ at $E/A=50$ MeV were detected in the exclusive 4π setup depicted in Fig. 1. Peripheral collisions were selected by the detection of forward-moving projectile-like fragments (PLFs). These PLFs were detected in the angular range $2.1^\circ \leq \theta^{lab} \leq 4.2^\circ$ and were identified in an annular Si(IP)/CsI(Tl)/PD ring detector (RD) by the ΔE -E technique. This telescope provided elemental identification with better than unit Z resolution for $Z \leq 48$, as shown in Fig. 2. The peak at $Z=48$ corresponds to quasi-elastically scattered projectile nuclei associated with the most peripheral collisions. The silicon ΔE element of this telescope was

segmented into 16 concentric rings on its junction side and 16 pie-shaped sectors on its ohmic surface. The ring segmentation provided a good measurement of the polar angle of the PLF, typically $\Delta\theta^{lab} < 0.2^\circ$, while the pie-shaped sectors allowed a measure of the azimuthal angle [11]. Careful calibration of the CsI(Tl) crystals with 70 fragmentation beams allowed determination of the light response of the CsI(Tl) crystals resulting in a typical energy resolution of 3%. From the measured Z , angle, and energy, the velocity of the PLF was calculated by assigning the A for a given Z consistent with systematics [22] adjusted near Z_{beam} to correspond to the N/Z of the projectile [23]. Intermediate mass fragments with $Z \leq 9$ and light-charged-particles were isotopically identified in the angular range $7^\circ \leq \theta^{lab} \leq 58^\circ$ with the high resolution silicon-strip array LASSA [24, 25]. Each of the nine telescopes in this array consisted of a stack of three elements, two ion-implanted, passivated silicon strip detectors (Si(IP)) backed by a 2×2 arrangement of CsI(Tl) crystals each with photo-diode readout. The second silicon of each telescope was segmented into 16 vertical strips and 16 horizontal strips, resulting in good angular resolution ($\Delta\theta^{lab} \approx 0.43^\circ$). The nine LASSA telescopes were arranged in a 3×3 array, the center of which was located at a polar angle $\theta^{lab} = 32^\circ$ with respect to the beam axis. The energy threshold of LASSA is 2 and 4 MeV/A for α particles and carbon fragments, respectively. A typical example of the isotopic resolution achieved by LASSA is shown in Fig. 3. Isotopes of Li and Be are clearly resolved with an energy resolution of ≈ 2 -5%. In order to augment the limited kinematical coverage of LASSA and the RD, the low-threshold Miniball/Miniwall array [26] was used to identify charged-particles emitted in the range $5^\circ \leq \theta^{lab} \leq 168^\circ$. Using pulse-shape discrimination, particles detected in the Miniball/Miniwall array were isotopically identified for $Z \leq 2$. These particles were used to select the impact parameter of the collision and to globally characterize the selected events.

III. GENERAL REACTION CHARACTERISTICS AND EVENT SELECTION

We begin by examining mid-peripheral (MP) events distinguished by the survival of a projectile-like fragment at forward angles. In order to examine these peripheral collisions we have selected events in which a heavy PLF with $30 \leq Z \leq 46$ is detected in the RD ($2.1^\circ \leq \theta^{lab} \leq 4.2^\circ$) coincident with at least three charged-particles in the Miniball/Miniwall array. This latter charged-particle requirement suppresses the most peripheral collisions and results in the associated multiplicity distribution shown in Fig. 4a. These MP collisions are characterized by an average total charged-particle multiplicity, $\langle N_C \rangle$, of 10.2, with a second moment (μ_2) of 3.6. Based on the charged-particle multiplicity distribution [27], we estimate the impact-parameter ratio $b/b_{max} \approx 0.7$ where

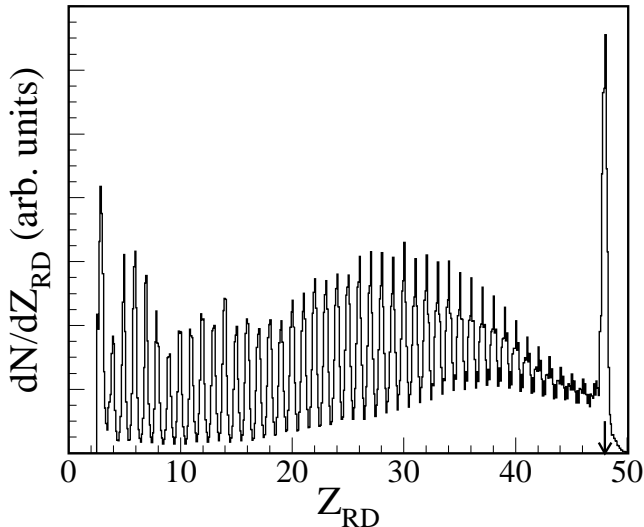


FIG. 2: Element distribution measured by the ring detector for the angular range $2.1^\circ \leq \theta^{lab} \leq 4.2^\circ$. The arrow indicates the atomic number of the beam.

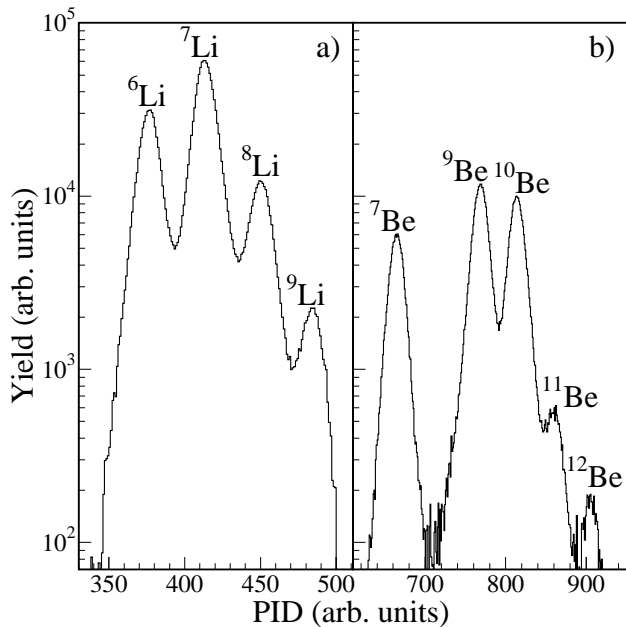


FIG. 3: Isotopic resolution achieved in LASSA for isotopes of Li and Be. The spectra have been summed over all nine LASSA telescopes.

b_{max} represents the interaction for which at least three charged-particles are detected in the Miniball/Miniwall array. The center-of-mass velocity distribution of the PLF detected in the RD is shown in Fig. 4b with the beam velocity indicated by an arrow for reference. One observes that this distribution is a skewed gaussian with a tail toward lower velocities. The most probable value

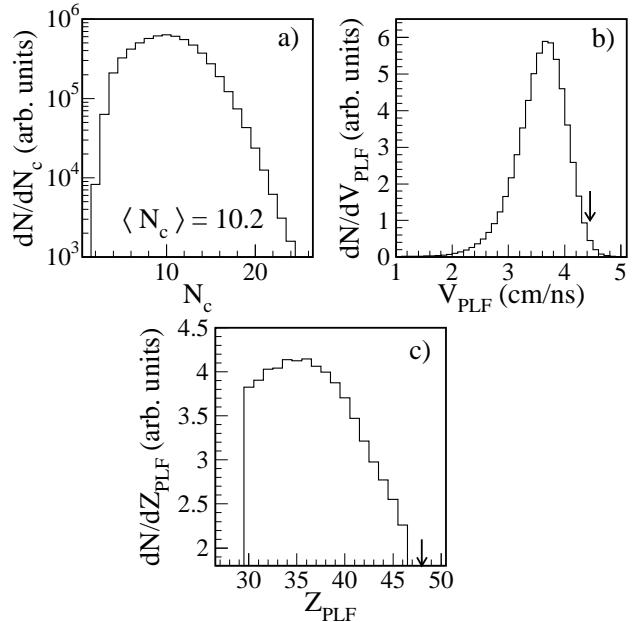


FIG. 4: Panel a) Charged-particle multiplicity distribution associated with the detection of a PLF with $30 \leq Z \leq 46$ in the RD; Panel b) Velocity distribution for $30 \leq Z \leq 46$ detected in RD; Panel c) Atomic number distribution of fragments detected in the RD.

of this velocity distribution is 3.7 cm/ns ($\langle V_{PLF} \rangle = 3.57$ cm/ns), indicating an average velocity damping of 0.88 cm/ns from the beam velocity. The atomic number distribution of PLFs associated with these collisions is displayed in Fig. 4c. The most probable value of Z_{PLF} is $Z = 35$ ($\langle Z_{PLF} \rangle = 37$) as compared to $Z_{beam} = 48$, indicated by the arrow. It should be realized that this most probable (or average) Z_{PLF} corresponds to the PLF following the de-excitation of the primary excited projectile-like fragment (PLF*).

The general characteristic of this de-excitation of the PLF* is shown in Fig. 5a. Clearly evident in Fig. 5a is a circular ridge of yield centered at $V_{\parallel} \approx 3.5$ cm/ns in the center-of-mass frame. This ridge can be understood as emission of ${}^6\text{Li}$ fragments from the PLF*, following the interaction phase of the reaction. This distinctive emission pattern indicates that for the collisions selected, a binary reaction has occurred [28]. By utilizing the measured multiplicities, kinetic energy spectra, and angular distributions of particles detected in coincidence with the PLF, we have reconstructed (under the assumption of isotropic emission) the average atomic number of the PLF*, $\langle Z_{PLF^*} \rangle$ and its excitation [29]. For the collisions studied, we have determined that $\langle Z_{PLF^*} \rangle \approx 41$. Also clearly evident in Fig. 5a, and well established by earlier work [9, 10], is that considerable fragment emission occurs at mid-velocity – emission *not* originating from the isotropic statistical decay of the PLF* or TLF* reaction partners [12]. For the remainder of this work we define

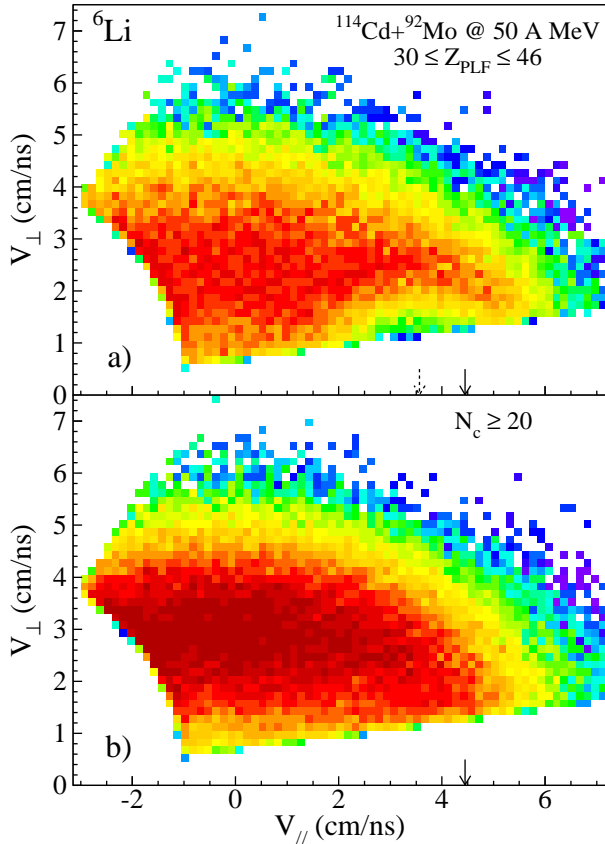


FIG. 5: (Color online) Invariant cross-section plots of the emission of ${}^6\text{Li}$ fragments in the center-of-mass frame. Panel a) associated with $30 \leq Z_{PLF} \leq 46$. Panel b) associated with $N_C \geq 20$. The dashed arrow indicates $\langle V_{\parallel}^{PLF} \rangle$ while the solid arrow indicates V_{BEAM} . The differential yield is presented on a logarithmic scale.

mid-velocity fragments as those with $0 \leq V_{\parallel} \leq 1 \text{ cm/ns}$ in the center-of-mass frame.

For central collisions ($N_C \geq 20$; $\langle N_C \rangle = 21.8$; $\mu_2 = 1.89$) the ridge centered near the projectile velocity is no longer observed, as shown in Fig. 5b. The observation that a clear Coulomb circle does not exist has traditionally been interpreted as evidence that the collision is no longer a binary process. However, the observation of a large charged particle multiplicity together with the absence of a Coulomb circle does not preclude the existence of a dissipative binary process. Rather, these observations can be reconciled with the rapid de-excitation of the PLF* and TLF* on a timescale commensurate with their re-separation. In contrast to the well defined Coulomb circle of Fig. 5a, the emission pattern for central collisions is broad and featureless with substantial emission near the center-of-mass velocity. In these collisions we deduce from the charged-particle multiplicity that $b/b_{max} = 0.26$, from which we estimate $Z_{source} \approx 72$ [30]. The charged-particle multiplicity has often been used in this manner to select central collisions. Examination of the Z distribution of the largest measured particle in the

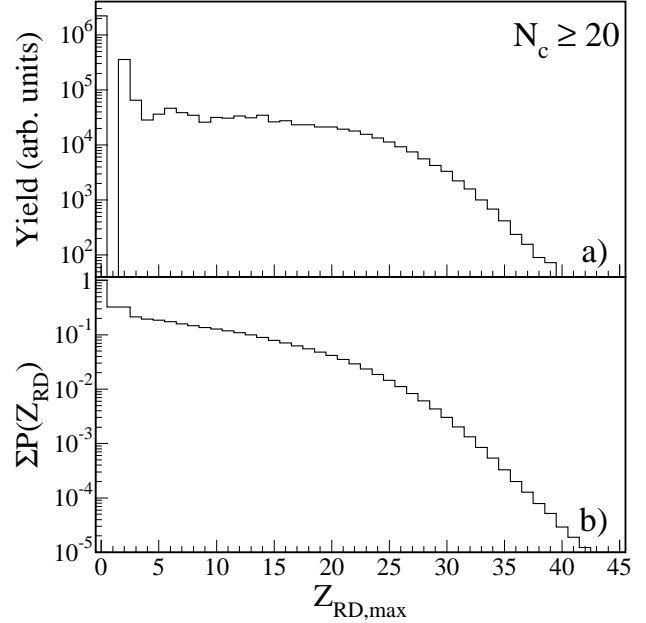


FIG. 6: Panel a) Z distribution of the largest fragment detected in the RD associated with events for which $N_C \geq 20$. Panel b) cumulative yield distribution of the largest fragment in the RD associated with events for which $N_C \geq 20$.

RD associated with these events, however, is quite revealing. As evident in Fig. 6a, while the largest probabilities are associated with either the detection of no fragment ($Z=0$) or a helium in the RD, there is a significant probability of detecting a large fragment with $Z \geq 10$ in the RD. (It should be noted that the triggering threshold in the RD was set to not trigger on hydrogen nuclei resulting in a measured yield of zero for $Z=1$ in Fig. 6a.) This detection of a large fragment ($Z \geq 10$) occurs even though a large charged-particle multiplicity has been required. This result is consistent with the physical picture of a large overlap of projectile and target nuclei which still results in a binary exit channel with survival of a projectile-like and target-like fragment. The cumulative yield associated with such events, $\Sigma P(Z_{RD})$, is shown in Fig. 6b where

$$\Sigma P(Z_{RD}) = \int_{Z=45}^{Z_i} \frac{dN}{dZ_{RD,max}} dZ \quad (1)$$

Evident in Fig. 6b is the result that $\Sigma P(Z_{RD}) \approx 0.1$ for $Z_{RD,max} = 10$. This result reveals that $\approx 10\%$ of the central collisions selected simply by the requirement that $N_C \geq 20$ are in fact associated with binary collisions. Due to the limited angular acceptance of the RD, this “contamination” of true central collisions might be somewhat higher.

Further evidence that this “contamination” is associated with a binary exit channel and not simply an anisotropic emission pattern is provided in Fig. 7. In this

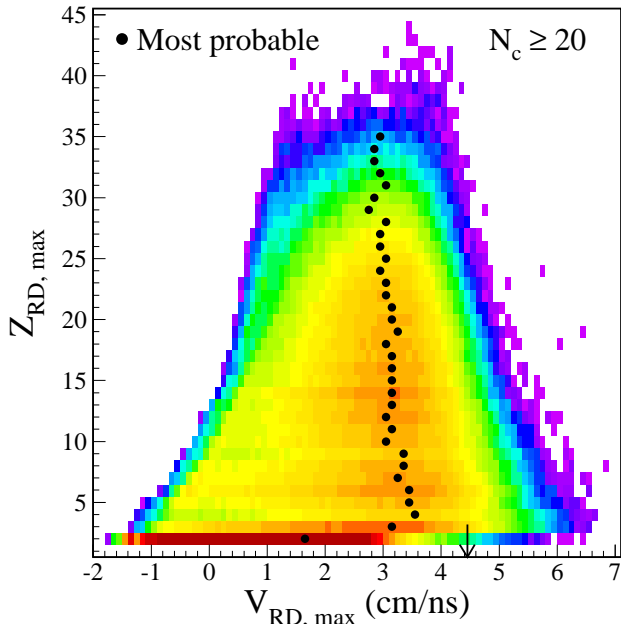


FIG. 7: (Color online) Correlation between atomic number and velocity (in the COM) of the largest fragment detected in the RD. The most probable velocity for each Z is indicated by a filled circle while the beam velocity is indicated by the arrow.

figure, we examine the correlation between the atomic number and the velocity of these fragments detected in the RD. With the exception of the lightest fragments ($Z \leq 3$), the fragments detected in the RD have a most probable velocity (indicated by the points) that is slightly damped from the beam velocity (indicated by the arrow). For $Z > 9$ the most probable velocity of the PLF is 3.1 cm/ns, corresponding to a damping of ≈ 1.3 cm/ns of the beam velocity. This “contamination” of true central events with dissipative binary events does not significantly affect any of our subsequent analysis. However, to provide the best isolation of true central events, we have additionally required in our selection of central events that no fragment with $Z \geq 5$ is detected in the RD.

IV. ELEMENTAL YIELDS

The Z distribution for IMFs associated with mid-peripheral (MP) and central (Cent) collisions for both PLF* emission and emission at mid-velocity is shown in Fig. 8. The observed yields in each case have been normalized for the range $3 \leq Z \leq 8$. To understand the Z distribution at mid-velocity ($0 \leq V_{\parallel} \leq 1$ cm/ns), we use PLF* emission (solid circles) as a reference. Fragments emitted from the PLF* were selected on the basis of their emission angle, θ^{PLF} , in the PLF frame ($85^{\circ} \leq \theta^{PLF} \leq 95^{\circ}$). For these same MP collisions, the Z distribution at mid-velocity (open triangles) exhibits a suppression of yield

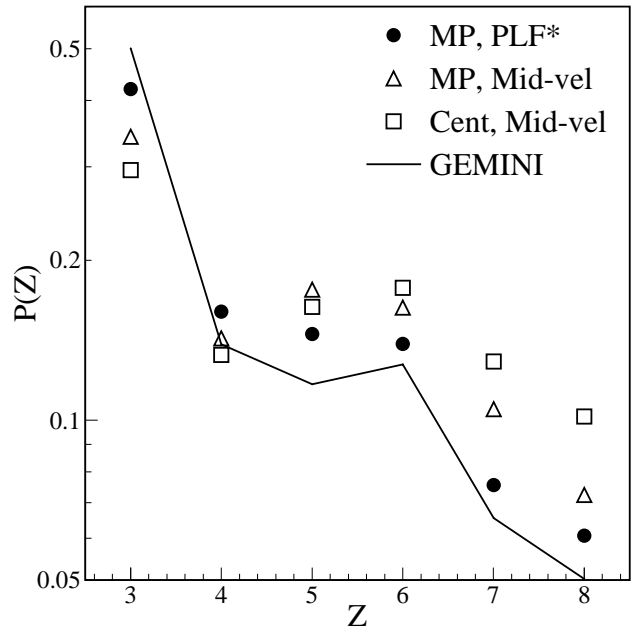


FIG. 8: Z distribution of fragments associated with mid-peripheral collisions emitted in the angular range $85^{\circ} \leq \theta^{PLF} \leq 95^{\circ}$ in the PLF frame (filled circles); mid-peripheral collisions and at mid-velocity (open triangles); and fragments associated with central collisions at mid-velocity (open squares). The lines depict the Z distribution predicted by the statistical model GEMINI (see text for details). The yield for each case has been normalized to unity for the interval shown.

for $Z=3$ and $Z=4$ relative to the production of heavier IMFs ($Z \geq 5$) as compared to PLF* emission (solid circles). This increase of the relative production of heavier IMFs at the expense of lighter IMFs is even larger for the case of central collisions (open squares). We conclude therefore that at mid-velocity (both in mid-peripheral and central collisions), heavier fragments are produced at the expense of lighter fragments, as compared to PLF* emission.

This change in the Z distribution at mid-velocity when compared to PLF* emission, can be understood within a statistical framework. Within such a framework, the Z distribution is influenced by the excitation, density, and size of the disintegrating system. Statistical emission of a fragment is governed by an effective emission barrier relative to the temperature of the emitting system. Increased relative probability for the emission of heavy fragments, can thus reflect either a reduction in this effective barrier and/or an increase in the temperature of the system. A reduction in the density of the emitting system naturally results in a reduction of the effective barrier. The Z distribution of mid-velocity fragments in mid-peripheral collisions is intermediate between that of PLF* emission and emission associated with central collisions. From this observation one may conclude that within a statistical

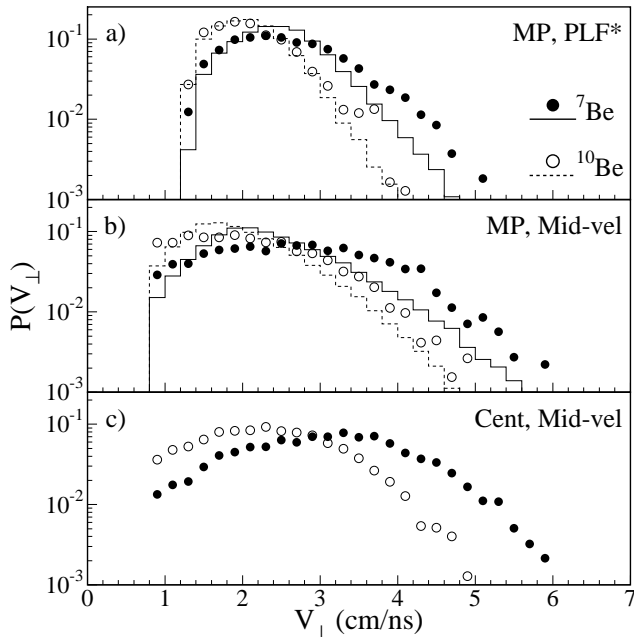


FIG. 9: Distributions of V_{\perp} , for ${}^7\text{Be}$ and ${}^{10}\text{Be}$ fragments in the center-of-mass frame. Panel a) mid-peripheral collisions and $V_{\parallel} \geq V_{\parallel}^{PLF^*}$; Panel b) mid-peripheral collisions and $0 \leq V_{\parallel} \leq 1$ cm/ns; Panel c) central collisions and $0 \leq V_{\parallel} \leq 1$ cm/ns. All distributions have been normalized to unity.

interpretation, the relative “energy cost” has already begun to change from that of the PLF*. At mid-velocity, the enhancement of yield for $Z \geq 6$ in the central case as compared to MP collisions may be due to the influence of finite source size. For MP collisions, the small size of the fragmenting system ($Z_{source} \approx 21$) at mid-velocity may limit the production of heavy IMFs.

V. TRANSVERSE VELOCITY DISTRIBUTIONS

We present in Figs. 9 and 10 the transverse-velocity distributions of ${}^{7,10}\text{Be}$ and ${}^{6,9}\text{Li}$ fragments. The different distributions correspond to fragments observed in different kinematical regions for mid-peripheral and central collisions. Depicted in Fig. 9a is the transverse-velocity distribution of ${}^7\text{Be}$ and ${}^{10}\text{Be}$ fragments which have parallel velocities larger than that of the PLF (in the PLF frame). Based on Fig. 5a we understand these fragments as being emitted from the PLF*. In this case, peaked distributions are observed as is expected from the Coulomb ‘ring’ observed in Fig. 5a, indicative of a well-defined Coulomb barrier characteristic of surface emission. The relative probability of neutron-rich ${}^{10}\text{Be}$ at low V_{\perp} is larger than that of neutron-deficient ${}^7\text{Be}$. It is important to note that the constraints of the experimental angular acceptance do not significantly impact the observed most probable velocity, an expectation confirmed by Coulomb trajectory calculations that will be

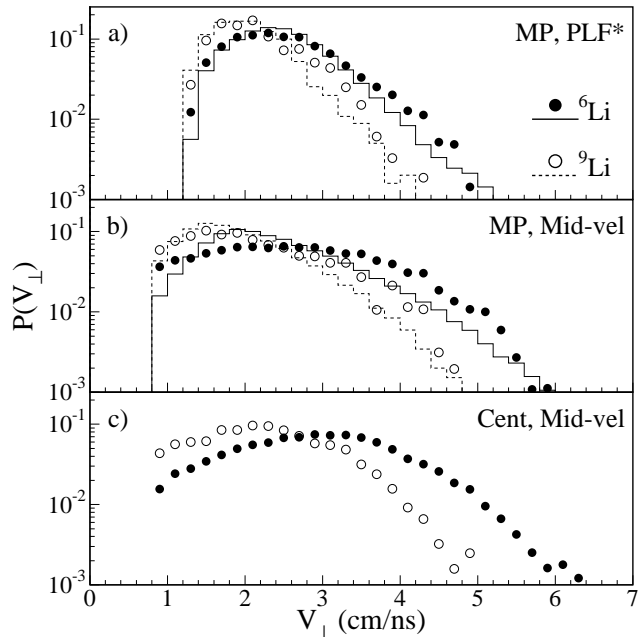


FIG. 10: Distributions of V_{\perp} , for ${}^9\text{Li}$ and ${}^6\text{Li}$ fragments in the center-of-mass frame. Panel a) mid-peripheral collisions and $V_{\parallel} \geq V_{\parallel}^{PLF^*}$; Panel b) mid-peripheral collisions and $0 \leq V_{\parallel} \leq 1$ cm/ns; Panel c) central collisions and $0 \leq V_{\parallel} \leq 1$ cm/ns. All distributions have been normalized to unity.

subsequently discussed. In contrast to the peaked distributions in Fig. 9a, the distributions associated with mid-velocity emission for mid-peripheral collisions (Fig. 9b) have broader peaks and extend to larger values of V_{\perp} . For $V_{\perp} \leq 2.5$ cm/ns, the V_{\perp} distribution for ${}^{10}\text{Be}$ in particular is essentially flat. The observation of large yield for low V_{\perp} indicates the absence of significant Coulomb repulsion in the transverse direction. Therefore, the observed V_{\perp} distributions reflect principally the initial V_{\perp} distributions. A broad and relatively flat initial V_{\perp} distribution is compatible with a neck-fragmentation scenario [31] or a Goldhaber picture in which the mid-velocity zone results from abrasion/ablation of nucleons between projectile and target nuclei followed by coalescence [32, 33]. The difference in the tails of the V_{\perp} distribution between PLF* emission and mid-velocity emission may be interpreted as the mid-velocity source having a higher initial temperature than the PLF* or possibly reflect the Fermi motion of the ablated nucleons.

Displayed in Fig. 9c are the V_{\perp} distributions for fragments emitted at mid-velocity in central collisions. These distributions also manifest broad peaks and high velocity tails *similar* to those observed in Fig. 9b. Close examination however reveals that in this case the V_{\perp} distribution is more peaked than in Fig. 9b suggesting that the Coulomb repulsion is larger in magnitude. This hypothesis is qualitatively consistent with the larger size (atomic number) of the source at mid-velocity for central collisions in contrast to mid-peripheral collisions. On the

other hand, the peak for the central case is broader than for the case of PLF* emission shown in Fig. 9a possibly indicating the volume breakup of a low-density source [34] or surface emission from a hot nucleus as it expands [35].

A semi-quantitative description of the V_{\perp} distributions presented in Fig. 9 can be achieved by comparing the experimental data with a N-body Coulomb trajectory model which simulates the superposition of multiple source emission. In this model, all emission was assumed to be surface emission originating from either the PLF* or a mid-velocity source. The characteristics of the PLF* were taken from the Z and energy directly measured, assuming the PLF* had the N/Z of the projectile. Event-by-event we assumed the Z of the mid-velocity source to be $Z_{mid-velocity} = Z_{system} - Z_{PLF^*}(1 + Z_T/Z_P)$. We determined $\langle Z_{mid-velocity} \rangle = 21$. Each source also has an associated temperature that is varied independently. The two sources were separated by an initial distance of 30 fm and were allowed to emit isotropically. Our use of surface emission in the mid-velocity case for mid-peripheral collisions simply provides an ansatz for performing the simulation and should not be interpreted as a physical description in this case. This particular choice of surface emission in the model notably affects the low-velocity region of the transverse-velocity spectrum. While a volume emission scenario results in a broader distribution, the shape of the spectrum in the high velocity region is largely unchanged.

This simple Coulomb model with $T_{PLF^*} = 7$ MeV provides a reasonable description of the PLF* emission as shown in Fig. 9a by the lines. Under-prediction of the tail of the ${}^7\text{Be}$ distribution by this simple model is most likely due to pre-equilibrium fragment emission processes, which are not included in the model. As thermal energy is the only source of initial kinetic energy in the model, reproducing the spectra depicted in Fig. 9b requires $T_{mid-velocity} = 20$ MeV. The physical origin of such a high temperature is unclear. The simulation also indicates that the contribution of TLF* emission to the mid-velocity region examined is insignificant. Analysis of the V_{\perp} distributions for Li isotopes reveals similar spectral shapes and slope parameters ($T_{PLF^*} = 7$ MeV and $T_{mid-velocity} = 20$ MeV) as shown in Fig. 10. Kinetic “temperatures” of similar magnitude have been previously reported for mid-velocity IMF emissions [13, 36].

It is noteworthy that both the ${}^7\text{Be}$ and ${}^{10}\text{Be}$, as well as the ${}^{6,9}\text{Li}$, spectra associated with mid-velocity emission, shown in Figs. 9 and 10, can be described with the same initial kinetic energy ($T_{mid-velocity} = 20$ MeV). The enhanced probability of low V_{\perp} emission as compared to the surface emission model may reflect temperature-dependent surface-entropy effects [37] or a transition from surface to volume emission [2].

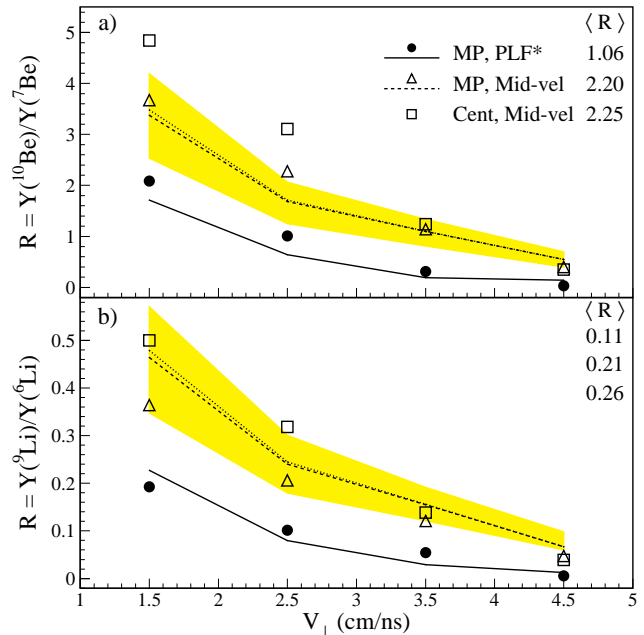


FIG. 11: Dependence of the ratios of ${}^{10}\text{Be}$ to ${}^7\text{Be}$ and ${}^9\text{Li}$ to ${}^6\text{Li}$ on V_{\perp} for different impact parameter and velocity selection criteria. Points displayed indicate the average value for $1 \leq V_{\perp} < 2$, $2 \leq V_{\perp} < 3$, $3 \leq V_{\perp} < 4$, and $V_{\perp} \geq 4$ cm/ns. Lines correspond to the predictions of a two source emission model. The shaded region corresponds to different assumptions for the neutron-enrichment of mid-velocity.

VI. ISOTOPIC COMPOSITION

The experimental observation that the transverse-velocity distributions for the neutron-rich (e.g. ${}^{10}\text{Be}$ and ${}^9\text{Li}$) isotopes are different from the neutron-deficient isotopes (e.g. ${}^7\text{Be}$ and ${}^6\text{Li}$) (Figs. 9 and 10) indicates that the ratio of these isotopes evolves as a function of V_{\perp} . In order to examine this dependence in a more transparent fashion, we examine the ratio of the yields of ${}^{10}\text{Be}$ to ${}^7\text{Be}$ as a function of V_{\perp} in Fig. 11a. For all three cases shown one observes that this ratio decreases monotonically with increasing V_{\perp} . For the case of PLF* emission (solid circles) this decrease can be simply understood as a consequence of the Coulomb barrier. As the Coulomb barrier for both ${}^{10}\text{Be}$ and ${}^7\text{Be}$ emission is similar, the ${}^7\text{Be}$, on average, acquires a higher velocity than the ${}^{10}\text{Be}$. The region of low V_{\perp} is therefore preferentially populated by the ${}^{10}\text{Be}$ as compared to the ${}^7\text{Be}$ as evident in Fig. 9a.

The most striking feature of Fig. 11a is that mid-velocity fragments associated with mid-peripheral collisions (open triangles) exhibit a significantly larger value of $Y({}^{10}\text{Be})/Y({}^7\text{Be})$ as compared to emission from the PLF* (solid circles). This enhancement is observed at all values of V_{\perp} . Mid-velocity fragments associated with central collisions (open squares) also manifest large values of $Y({}^{10}\text{Be})/Y({}^7\text{Be})$, as compared to emission from the PLF*. The yield ratios associated with central colli-

sions are even larger than those mid-velocity emission in the mid-peripheral case (open triangles), however most of this difference occurs for low V_{\perp} ($V_{\perp} \leq 2.5$ cm/ns). This V_{\perp} dependence of $Y(^{10}\text{Be})/Y(^7\text{Be})$ for both PLF* emission and mid-velocity emission can explain the angular dependence of neutron-deficient fragments previously reported [38]. As different Coulomb repulsion in the different cases leads to different behavior of the yield ratio as a function of V_{\perp} , it is important to compare the yield ratios integrated over V_{\perp} .

By integrating over the entire range of V_{\perp} observed, we find that $\langle Y(^{10}\text{Be})/Y(^7\text{Be}) \rangle$ for PLF* emission is 1.06 while at mid-rapidity it is considerably higher, 2.2 for mid-peripheral collisions and 2.25 for central collisions. Based upon these integrated yields, one observes that for Be,

$$\frac{R_{\text{mid-velocity,mid-peripheral}}}{R_{\text{PLF*,mid-peripheral}}} = \frac{2.2}{1.06} = 2.08 \quad (2)$$

while

$$\frac{R_{\text{mid-velocity,central}}}{R_{\text{PLF*,mid-peripheral}}} = \frac{2.25}{1.06} = 2.12 \quad (3)$$

Thus, the integrated yield of $^{10}\text{Be}/^7\text{Be}$ at mid-velocity for mid-peripheral and central collisions is comparable and significantly different from PLF* emission. The behavior exhibited by the $Y(^{10}\text{Be})/Y(^7\text{Be})$ is also observed for $Y(^9\text{Li})/Y(^6\text{Li})$, as shown in the lower panel of Fig. 11. It is remarkable that at mid-velocity not only are the Z and transverse-velocity distributions similar for mid-peripheral and central collisions, but the fragment composition is essentially the same – while markedly different from PLF* emission.

It is important to consider the influence of the PLF* Coulomb field on the observed N/Z enrichment at mid-velocity. Radial repulsion of fragments from the PLF* results in ^7Be fragments displaced more toward mid-velocity than ^{10}Be fragments. Therefore the Coulomb field of the PLF* and TLF* lead to an increase in the yield of neutron-deficient isotopes at mid-velocity. Hence, due to these qualitative arguments the primordial N/Z composition at mid-velocity is expected to be higher than that experimentally observed.

The N-body Coulomb trajectory model previously described can also be used to quantify this enhancement of $Y(^{10}\text{Be})/Y(^7\text{Be})$ at mid-velocity as compared to PLF* emission. The relative emission probability, $Y(^{10}\text{Be})/Y(^7\text{Be})$, for the PLF* was taken from the experimental data while for the mid-velocity source this probability was taken relative to the PLF* ratio as $K \cdot Y_{\text{PLF*}}(^{10}\text{Be})/Y_{\text{PLF*}}(^7\text{Be})$, where K was varied as a free parameter. For mid-peripheral collisions, the superposition of PLF* emission and emission of the mid-velocity source with $V_{\parallel} > V_{\parallel}^{\text{PLF*}}$ in the model is indicated by the solid line in Fig. 11, while the corresponding yield at mid-velocity is represented by the dashed line. Reproducing the V_{\perp} dependence of the relative

yield, requires consideration of both the Coulomb repulsion from the emitting source, and the initial velocities of the fragments. Accounting for the initial velocities in a realistic manner is accomplished by attributing a temperature to the emitting source. In the case of emission from the PLF* we use, consistent with the V_{\perp} of Fig. 9a, a temperature of $T_{\text{PLF*}}=7$ MeV to model the PLF* decay. The solid line presented in Fig. 11 reflects predominantly the emission from the PLF*. Reproducing the mid-velocity data necessitates that $Y_{\text{mid-velocity}}(^{10}\text{Be}/^7\text{Be})=2 \cdot Y_{\text{PLF*}}(^{10}\text{Be}/^7\text{Be})$ and that $T_{\text{mid-velocity}}=20$ MeV. These latter temperatures are also consistent with those deduced from the V_{\perp} distributions shown in Figs. 9 and 10. Shown as the shaded region in Fig. 11 is the sensitivity of the yield ratio to the parameter K . The bottom of the shaded region corresponds to $K=1.5$ while the top corresponds to $K=2.5$. While the dashed line represents the superposition of mid-velocity and PLF* emission, the dotted line depicts the contribution of only the mid-velocity source. While the dotted line is only slightly higher than the dashed line, this difference is sensitive to the assumption of isotropic emission from the PLF*. Enhanced backward emission from the PLF*, as has recently been reported [39], would correspondingly result in a larger difference. All the trends described for $Y(^{10}\text{Be})/Y(^7\text{Be})$ are also observed for $Y(^9\text{Li})/Y(^6\text{Li})$, as shown in Fig. 11b, supporting the conclusion that the $Y(^{10}\text{Be})/Y(^7\text{Be})$ ratio is not an isolated case but is representative of other fragments. To extract more quantitative information on the relative yield enhancement at mid-velocity, it is necessary to more accurately account for the “distortion” introduced by the presence of the PLF* and TLF*. The distortion, particularly important for low V_{\perp} , depends on the IMF emission rates relative to the PLF*-TLF* re-separation and is beyond the scope of the present analysis.

VII. GEMINI CALCULATIONS

To understand the PLF* decay better, we performed calculations with the statistical-model code GEMINI [40], which describes surface emission from an excited nucleus including emission from excited states and their sequential decay. We examined the isotopic yields as a function of the excitation and spin of a parent nucleus. At each excitation energy we roughly reproduce the average atomic number of the measured PLF. In Table I, for a fixed J one observes that the $Y(^{10}\text{Be})/Y(^7\text{Be})$ decreases with increasing E^*/A , while for fixed E^*/A , it increases with increasing J . For $J = 0\hbar$ to reproduce the measured value of 1.06 associated with PLF* emission, we deduce an excitation of $E^*/A \approx 3\text{-}4$ MeV. As the level density is taken to be $a=A/9$ MeV $^{-1}$ in the model, this excitation corresponds to a temperature of $T \approx 6$ MeV, in reasonable agreement with the tails of the transverse-velocity distribution. If the PLF* has significant spin ($\approx 20\hbar$), the temperature of the source must be some-

$E^*/A(\text{MeV})$	$J=0\hbar$	$J=20\hbar$	$J=40\hbar$
2	1.50	>1.8	4.67
3	1.29	1.14	2.11
4	0.78	1.17	1.42

TABLE I: Results of GEMINI calculations indicating the dependence of $Y(^{10}\text{Be})/Y(^7\text{Be})$ on excitation energy, E^*/A , and spin, J , for emission from the PLF* ($Z \approx 40-48$, $N/Z \approx 1.375$).

what higher. Thus, within a surface emission picture the $Y(^{10}\text{Be})/Y(^7\text{Be})$ and the transverse-velocity distributions constrain the excitation and spin of the emitting source. Correctly accounting for the interplay of both of these quantities is necessary to describe the conditions of the emitting source. For these conditions ($Z=48$, $A=114$, $E^*/A=3.5$ MeV, $J=0\hbar$), we have compared the yield distribution of fragments predicted by GEMINI with that observed for PLF* emission. The solid line shown in Fig. 8 is the GEMINI yield distribution normalized to the range $3 \leq Z \leq 8$. While in general the agreement between the GEMINI calculations and emission from the PLF* is reasonable, GEMINI overpredicts the relative yield of $Z=3$ while under-predicting the relative yield for $Z \geq 4$. An improved description of PLF* emission could be done with a meta-stable mononuclear model which accounts for its expansion [41]. While this may affect the overall emission probabilities, such a treatment is unlikely to affect the ratios presently discussed.

VIII. Z AND A DEPENDENCE OF $\langle E_{\perp} \rangle$

The average transverse energies of $2 \leq Z \leq 6$ fragments are displayed in Fig. 12 for different impact parameter and velocity selection criteria. To examine emission from the PLF* without being biased by the minimum angular acceptance of LASSA, we have selected emission for $85^\circ \leq \theta^{PLF} \leq 95^\circ$ in the PLF frame. The values of $\langle E_{\perp} \rangle$ for these different selections can be understood in the context of a simple physical picture in which fragments acquire their transverse kinetic energy as a result of Coulomb repulsion, thermal motion, and possibly energy associated with collective expansion [42]. As the thermal component is mass (Z) independent, an observed Z dependence can be attributed to Coulomb repulsion of fragments from the emitting PLF* or the presence of collective motion [42]. Distinguishing between the Z and A dependence of the $\langle E_{\perp} \rangle$ can differentiate between the Coulomb and collective contributions to the transverse energy. In the case of emission from the PLF* (solid circles), the measured average transverse kinetic energies in the PLF frame generally increase with Z . The magnitude of $\langle E_{\perp} \rangle$ for $Z=2$ is roughly consistent with values previously reported for a similar system [43]. These measured magnitudes of $\langle E_{\perp} \rangle$ can be understood within a surface emission picture in which

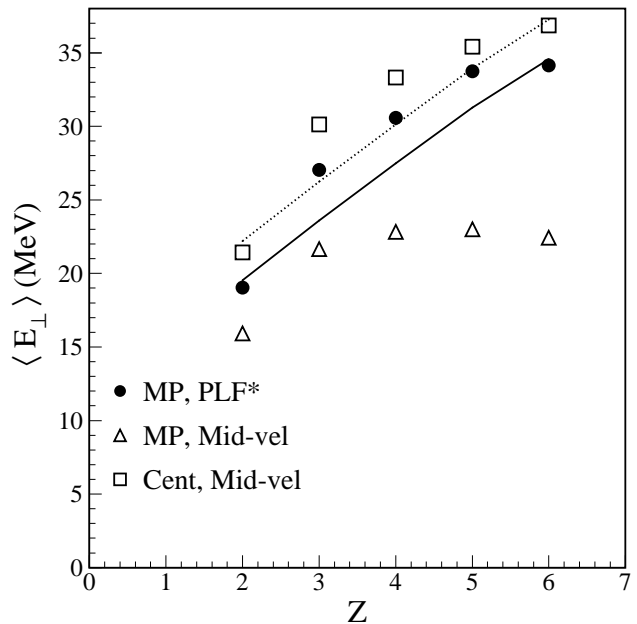


FIG. 12: Average transverse energies for $2 \leq Z \leq 6$ selected under different criteria. For the PLF*, fragments were selected in the angular range $85^\circ \leq \theta^{PLF} \leq 95^\circ$ while mid-velocity fragments have $0 \leq V_{\parallel} \leq 1 \text{ cm/ns}$ in the center-of-mass frame.

fragments are emitted from the surface of a hot nucleus. The $\langle E_{\perp} \rangle$ in such a picture is given by $\langle E_{CM} \rangle = \langle V_C \rangle + 2 \langle T \rangle$ where the Coulomb energy $V_C = 1.44 (Z_{source} - Z_{fragment}) * Z_{fragment} / R$ with R , the center-to-center separation distance between the fragment and source, taken as $R = 1.2 * ((A_{source} - A_{fragment})^{1/3} + A_{fragment}^{1/3}) + 2$ fm. The average Coulomb energy has been calculated within this simple picture. The corresponding $\langle E_{\perp} \rangle$ ($\langle E_{\perp} \rangle = \frac{2}{3} \langle E_{CM} \rangle$) for a temperature of $T=7$ MeV is indicated by the solid line in Fig. 12 while $T=9$ MeV is represented by the dotted line. The magnitude of the observed $\langle E_{\perp} \rangle$ and the dependence on Z is qualitatively described by this simple model, bolstering the view that this emission is standard statistical emission from a near normal density PLF*.

In Fig. 12, a marked contrast between emission from the PLF* and fragments at mid-velocity associated with mid-peripheral collisions (open triangles) is observed. Mid-velocity fragments in MP collisions manifest significantly lower $\langle E_{\perp} \rangle$ in the PLF frame and for $3 \leq Z \leq 6$ essentially no dependence of $\langle E_{\perp} \rangle$ on Z exists. The $\langle E_{\perp} \rangle$ for helium is approximately 25-30% lower than for IMFs. The magnitude of $\langle E_{\perp} \rangle$ for $3 \leq Z \leq 6$ is ≈ 22 MeV, essentially 2/3 of the Fermi energy. The magnitude of $\langle E_{\perp} \rangle$ for $Z=2$ is ≈ 16 MeV. $\langle E_{\perp} \rangle$ values of similar magnitude at mid-velocity have previously been reported for IMFs, integrated over Z , and neutron-rich light-charged-particles for a significantly lighter system [44]. This independence on Z , together with the fact that the $\langle E_{\perp} \rangle$ is approximately 2/3 the Fermi energy suggests that the trans-

verse energy of these fragments does not contain any significant Coulomb contribution, as was previously conjectured based upon the V_{\perp} distribution shown in Figs. 9 and 10. This result is consistent with a physical picture in which fragments aggregate in a dilute nuclear medium – compatible with a Goldhaber scenario as has been previously suggested [36]. Both the Z independence of $\langle E_{\perp} \rangle$ and the reported magnitudes in the present work are consistent with those previously reported [36]. Alternatively, this behavior can be viewed as the volume breakup of a low-density source or as emission from a distended configuration. On the basis of transverse energies, it has been proposed [13, 36] that fragments intermediate between the PLF* and TLF* are dynamical in nature, maintaining early-stage correlations of the collision [45].

For mid-velocity fragments associated with central collisions (open squares), examination of the dependence of $\langle E_{\perp} \rangle$ on Z , and in particular the magnitudes of the measured $\langle E_{\perp} \rangle$ is particularly revealing. For this case, $\langle E_{\perp} \rangle$ increases monotonically with Z , indicating a Coulomb influence. For $Z=2$, the value measured in this work is consistent with values previously reported [43]. The magnitude of $\langle E_{\perp} \rangle$, however, is only slightly larger than in the case of emission from the PLF* (solid circles). These two cases, however, involve significantly different charge associated with the emitting system. For central collisions the initial atomic number of the mid-velocity source is almost double that of the PLF* ($Z_S=72$ as compared to $Z_{PLF^*}=41$). Hence, the similarity of the values of $\langle E_{\perp} \rangle$ for central collisions with those for emission from the PLF* suggests that for central collisions, fragments originate either from a dilute nuclear system (either volume breakup or surface emission during expansion), or after considerable charge has been removed from the system, by fast, light-charged-particle emission. The large Coulomb barrier for IMF emission favors early emission of IMFs making IMF emission following light-charged-particle de-excitation, on average, less likely.

To disentangle the contribution of Coulomb energy and any possible collective flow [42] to the $\langle E_{\perp} \rangle$, we examine the dependence of $\langle E_{\perp} \rangle$ on A for individual elements in Fig. 13. Significant collective expansion effects have been previously asserted [17, 46], particularly for the case of central collisions. Evident in panel a) for the case of central collisions is that for IMFs, in the case of $N \geq Z$, the observed $\langle E_{\perp} \rangle$ does not increase with increasing A for a given Z but is either constant or decreases slightly. This observation contradicts the expectation of a mass-dependent collective flow, at least in the transverse direction. The most striking feature of Fig. 13a is that neutron-deficient isotopes, particularly ${}^3\text{He}$, ${}^7\text{Be}$, and ${}^{11}\text{C}$, exhibit larger $\langle E_{\perp} \rangle$ than other isotopes of the same element. For ${}^6\text{Li}$ essentially no enhancement is observed while for ${}^{10}\text{B}$ only a modest enhancement is observed. One possible reason for this difference between odd and even Z is that only for even- Z are nuclides with $N < Z$ observed with significant yield. This enhancement in the kinetic energy of neutron-deficient fragments in

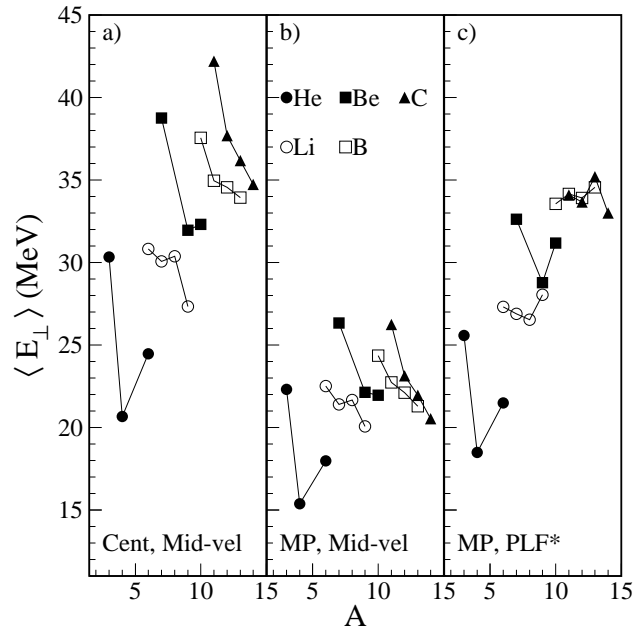


FIG. 13: Average transverse energies as a function of mass number for $2 \leq Z \leq 6$ for mid-peripheral and central collisions with different selection criteria. For the PLF*, fragments were selected in the angular range $85^\circ \leq \theta^{PLF} \leq 95^\circ$ while mid-velocity fragments have $0 \leq V_{\parallel} \leq 1 \text{ cm/ns}$ in the center-of-mass frame.

comparison to other isotopes of the same element has been previously reported for central collisions in the system ${}^{112}\text{Sn} + {}^{112}\text{Sn}$ at $E/A=50$ MeV and has been interpreted as evidence for surface emission from a hot, expanding nuclear system [47]. It has been hypothesized that the larger kinetic energy observed for the neutron-deficient isotopes originates because they are emitted on average earlier than other isotopes of the same element [47].

In contrast to the previous work which focused solely on central collisions [47], we also present the dependence of $\langle E_{\perp} \rangle$ associated with mid-peripheral collisions for both emission from the PLF* and the mid-velocity regime. In the case of mid-velocity we observe the same effect as for central collisions, although the magnitude of the enhancement is somewhat less. As the physical picture of a hot, source which emits as it expands is not compatible with the case of mid-velocity emission for mid-peripheral collisions, the observed trend must have an alternate explanation. In the case of emission from the PLF*, ${}^{11}\text{C}$ does *not* show an enhancement in contrast to the two mid-velocity cases, emphasizing the difference between mid-velocity fragment production and emission from the PLF*. A significant enhancement of the average kinetic energy is still observed for ${}^3\text{He}$ and ${}^7\text{Be}$ emitted from the PLF*. Thus, this kinetic enhancement of neutron-deficient isotopes is not associated simply with central collisions in which a low density, expanded source is formed but also

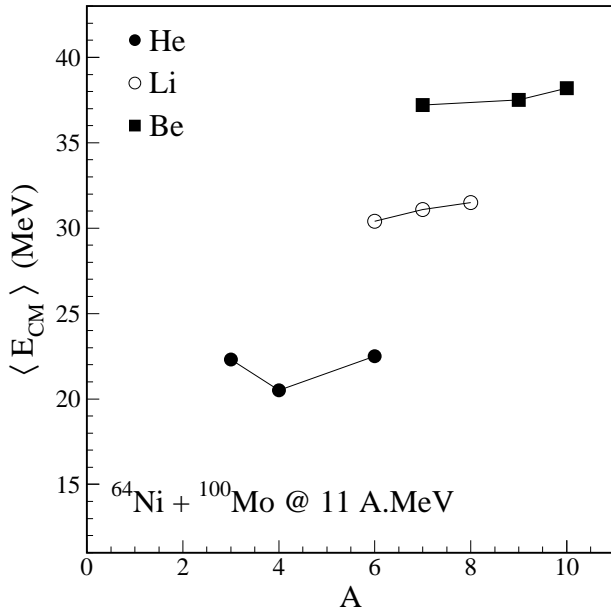


FIG. 14: Average center-of-mass energies for $2 \leq Z \leq 4$ as a function of mass selected by element following incomplete fusion in the reaction $^{64}\text{Ni} + ^{100}\text{Mo}$ at $E/A=11$ MeV [40].

occurs in the standard statistical decay of a near normal density PLF*.

If the observed effect is related to a displacement in the emission time distributions of neutron-deficient isotopes with respect to heavier isotopes of the same element [47], one would expect the effect to decrease with increasing excitation energy as the system moves toward instantaneous breakup [2]. As a baseline for a nuclear system at relatively low excitation, we have examined helium isotopes and IMFs emitted in the reaction $^{64}\text{Ni} + ^{100}\text{Mo}$ at $E/A=11$ MeV [40]. Following incomplete fusion of the projectile Ni nuclei with the Mo target nuclei, evaporation residues were measured in coincidence with emitted neutrons, charged particles, and IMFs detected at selected angles. The kinetic energy spectra of these emitted particles is clearly evaporative. On the basis of its velocity, the excitation of the evaporation residue is estimated to be $E^*=319 \pm 27$ MeV [48]. Thus, this system provides an important low-excitation reference point in a system of comparable Z and A to the central collision data of the present work. The dependence of $\langle E_{CM} \rangle$ on A is shown in Fig. 14. Clearly evident in this figure is the fact that standard statistical emission at low excitation *does not* result in a large enhancement of the kinetic energies of the neutron-deficient isotopes ^3He and ^7Be . A difference of ≈ 2 MeV is observed between the ^3He and ^4He average kinetic energies. Due to the low excitation energy of this system, sequential feeding of ^3He is expected to be negligible. Consequently, the observed energy difference between ^3He and ^4He can be largely attributed to the earlier average emission time of ^3He . This difference pro-

vides a reference point for the increase in cluster kinetic energy due to differences in the average emission time. The large difference observed in average kinetic energies of neutron-deficient isotopes in the $^{114}\text{Cd} + ^{92}\text{Mo}$ system is therefore not principally due to differences in the average emission time of fragments.

Direct evidence that the excitation of the emitting source is primarily responsible for the enhancement of the neutron deficient isotopes is presented in Fig. 15 for emission from the PLF*. In panel a) the $\langle E_{\perp} \rangle$ for isotopes of helium are shown as a function of the PLF velocity. For this portion of the analysis we expand our definition of the PLF to include $15 \leq Z_{PLF} \leq 46$ [29]. It has previously been demonstrated that the velocity damping of the PLF* is associated with the excitation incurred in the PLF* following the interaction phase of the collision [29]. The deduced excitation energy scale is indicated at the top of the figure while the beam velocity is represented by an arrow. As $\langle V_{PLF} \rangle$ decreases from the beam velocity (excitation energy increases) the $\langle E_{\perp} \rangle$ for ^3He , ^4He , and ^6He all increase monotonically. To explore the differences between the increase in kinetic energy for the different helium isotopes in a more sensitive manner, we examined the increase in the $\langle E_{\perp} \rangle$ for ^3He and ^6He relative to ^4He . These results are presented in the lower panel of Fig. 15. The difference in transverse energy between ^3He and ^4He increases with increasing excitation from 5.7 MeV at $\langle E^*/A \rangle \approx 2$ MeV to 9.3 MeV at $\langle E^*/A \rangle \approx 5.8$ MeV. On the other hand, aside from an initial decrease, the transverse energy difference between ^6He and ^4He relative remains approximately constant over the measured range. We emphasize that the average kinetic energy enhancement for neutron-deficient isotopes increases with increasing excitation energy (solid stars), opposing the expected behavior based upon an emission time displacement argument.

These observations may be qualitatively understood by considering the growing importance of charged-particle decay channels with increasing excitation energy. A fragment emitted from a hot source with an initial thermal energy accelerates in the Coulomb field of the emitting system and acquires its asymptotic kinetic energy. If this fragment decays by neutron emission, the velocity of the secondary fragment is on average the same as the primary fragment at the moment of decay, thus its observed kinetic energy is only impacted by the change in mass. However, should the fragment undergo charged-particle decay, then the kinetic energy observed for the secondary fragment reflects the Coulomb energy acquired by its parent up to the moment of decay, which is larger due to the larger parent atomic number. *Only if* the lifetime of the parent is sufficiently long for it to transform a significant fraction of its initial Coulomb energy into kinetic energy will the kinetic energy of the daughter fragment be appreciably increased. Instantaneous decay of the parent fragment will not result in an increase in the kinetic energy of the daughter fragments. This physical picture suggests that the neutron-deficient iso-

IX. CONCLUSIONS

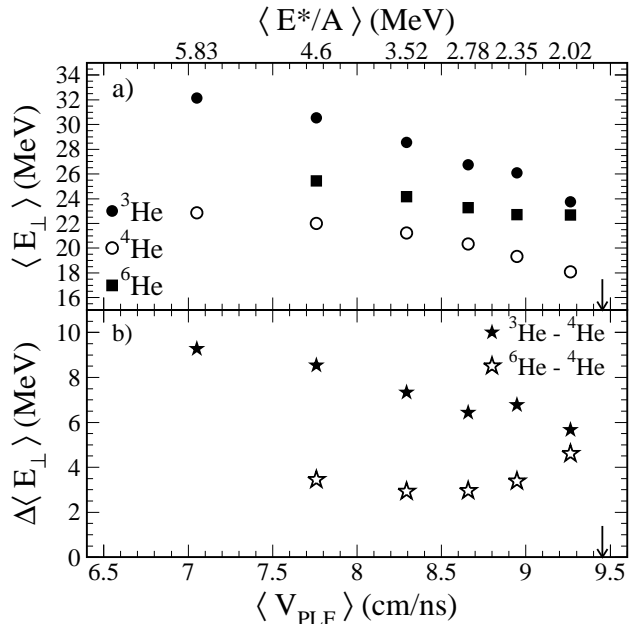


FIG. 15: Panel a) $\langle E_{\perp} \rangle$ for helium isotopes as a function of $\langle V_{PLF} \rangle$ and deduced excitation energy (upper axis). ${}^3\text{He}$ (solid circles), ${}^4\text{He}$ (open circles), and ${}^6\text{He}$ (solid squares). Panel b) Average transverse energy of ${}^3\text{He}$ and ${}^6\text{He}$ with reference to ${}^4\text{He}$.

topes manifest a secondary decay contribution from relatively long-lived charged-particle channels, i.e narrow resonances at relatively low excitation in the parent fragment. It is therefore clear from the evidence presented that the fragments are not created relatively cold as predicted in some multi-fragmentation models [49]. Moreover, these hot fragments do not decay instantaneously. Measurement of the yield associated with multi-particle resonant decay would provide quantitative information about this scenario. Unfortunately, the present experimental data does not allow examination of these resonant decays. With increasing excitation, the secondary decay feeding to ${}^3\text{He}$ and ${}^4\text{He}$ changes, presumably affects the yield ratios of the two isotopes a reference benchmark for isotope thermometry [50, 51]. It should be realized that independent of the underlying origin of the kinetic energy difference, there is an inherent danger of examining double ratios such as $(Y({}^3\text{He})/Y({}^4\text{He})) / (Y({}^6\text{Li})/Y({}^7\text{Li}))$ involving only one isotope with $N < Z$ that manifests a considerably different kinetic energy. Our results may also suggest that extracting the primordial N/Z to investigate the possible isospin fractionation of a dilute nuclear medium requires detailed measurement of both neutron and charged-particle resonant decays.

In summary, it is revealing to compare the characteristics of mid-velocity fragments and those emitted in the de-excitation of a hot, near-normal density nucleus, namely the PLF*. The Z distributions and the transverse-velocity distributions, for mid-velocity emission are different from those associated with PLF* emission. On the other hand, fragments observed at mid-velocity are rather similar independent of whether they are associated with mid-peripheral or central collisions. The integrated yield ratios of ${}^{10}\text{Be}/{}^7\text{Be}$ and ${}^9\text{Li}/{}^6\text{Li}$ reveal that mid-velocity and PLF* emission are also substantially different in N/Z . For central collisions and mid-peripheral collisions, these observed yield ratios are enhanced by a factor of approximately two with respect to PLF* emission. In the case of emission from the PLF*, the Z dependence of $\langle E_{\perp} \rangle$ shows that fragment emission is *consistent* with standard evaporation from near normal density nuclear matter. In central collisions the Z dependence and magnitude of $\langle E_{\perp} \rangle$ for mid-velocity fragments are *inconsistent* with normal density formation. For mid-velocity fragments formed in mid-peripheral collisions, the Z independence of $\langle E_{\perp} \rangle$ and a magnitude of approximately two-thirds of the Fermi energy, suggest cluster formation through coalescence of ablated nucleons. All these facts are consistent with the low-density formation of fragments at mid-velocity for both mid-peripheral and central collisions, indicating that the conditions for fragment formation at mid-velocity are *significantly different from those of PLF* emission*. Examination of $\langle E_{\perp} \rangle$ for isotopically identified fragments shows that neutron-deficient isotopes, particularly those with $N < Z$, exhibit larger kinetic energies than heavier isotopes of the same element. This enhancement of the kinetic energies for neutron-deficient isotopes increases with increasing excitation energy. This result suggests that fragments are produced hot and that long-lived charged-particle decay may be important for $N < Z$ clusters, motivating the future study of resonant decay.

Acknowledgments

We would like to acknowledge the valuable assistance of the staff at MSU-NSCL for providing the high quality beams which made this experiment possible. This work was supported by the U.S. Department of Energy under DE-FG02-92ER40714 (IU), DE-FG02-87ER-40316 (WU) and the National Science Foundation under Grant No. PHY-95-28844 (MSU).

[1] L. G. Sobotka et al., Phys. Rev. Lett. **51**, 2187 (1983).
 [2] L. Beaulieu et al., Phys. Rev. Lett. **84**, 5971 (2000).

[3] R. T. deSouza et al., Phys. Lett. B **268**, 6 (1991).
 [4] D. R. Bowman et al., Phys. Rev. Lett. **67**, 1527 (1991).

- [5] C. A. Ogilvie et al., Phys. Rev. Lett. **67**, 1214 (1991).
- [6] G. F. Peaslee et al., Phys. Rev. C **49**, 2271(R) (1994).
- [7] U. Milkau et al., Phys. Rev. C **44**, 1242(R) (1991).
- [8] Y. D. Kim et al., Phys. Rev. Lett. **67**, 14 (1991).
- [9] J. Töke et al., Phys. Rev. Lett. **75**, 2920 (1995).
- [10] E. Plagnol et al., Phys. Rev. C **61**, 014606 (2000).
- [11] B. Davin et al., Phys. Rev. C. **65**, 064614 (2002).
- [12] F. Bocage et al., Nucl. Phys. A. **676**, 391 (2000).
- [13] S. Piantelli et al., Phys. Rev. Lett. **88**, 052701 (2002).
- [14] J. Colin et al., Phys. Rev. C **67**, 064603 (2003).
- [15] H. S. Xu et al., Phys. Rev. Lett. **85**, 716 (2000).
- [16] P. M. Milazzo et al., Phys. Rev. C. **66**, 021601R (2002).
- [17] N. Marie et al., Phys. Lett. B **391**, 15 (1997).
- [18] M. Colonna et al., Phys. Rev. Lett. **88**, 122701 (2002).
- [19] T. Sil et al., Phys. Rev. C **69**, 014602 (2004).
- [20] J. F. Dempsey et al., Phys. Rev. C **54**, 1710 (1996).
- [21] Y. Laroche et al., Phys. Rev. C **62**, 051602 (2000).
- [22] K. Summerer et al., Phys. Rev. C **42**, 2546 (1990).
- [23] B. Davin, PhD Thesis **Indiana University** (2001).
- [24] B. Davin et al., Nucl. Instr. and Meth. **A473**, 302 (2001).
- [25] A. Wagner et al., Nucl. Instr. and Meth. **A456**, 290 (2001).
- [26] R. T. de Souza et al., Nucl. Instr. and Meth. **A295**, 109 (1990).
- [27] C. Cavata et al., Phys. Rev. C **42**, 1760 (1990).
- [28] B. Lott et al., Phys. Rev. Lett. **68**, 3141 (1992).
- [29] R. Yanez et al., Phys. Rev. C. **68**, 011602(R) (2003).
- [30] H. Xu et al., Phys. Rev. C **65**, 061602(R) (2002).
- [31] U. Brosa and S. Grossmann, J. Phys. G **10**, 933 (1984).
- [32] A. S. Goldhaber, Phys. Lett. B **53**, 306 (1974).
- [33] K. Hagel et al., Phys. Rev. C. **62**, 034607 (2000).
- [34] E. R. Foxford et al., Phys. Rev. C **54**, 749 (1996).
- [35] W. Friedman, Phys. Rev. C **42**, 667 (1990).
- [36] J. Lukasik et al., Phys. Rev. C **66**, 064606 (2002).
- [37] J. Töke et al., Phys. Rev. C **67**, 034609 (2003).
- [38] E. Ramakrishnan et al., Phys. Rev. C **57**, 1803 (1998).
- [39] S. Hudan et al., Phys. Rev. C **70**, 031601(R) (2004).
- [40] R. J. Charity et al., Phys. Rev. C. **63**, 024611 (2001).
- [41] L. G. Sobotka et al., Phys. Rev. Lett. **93**, 132702 (2004).
- [42] R. T. deSouza et al., Phys. Lett. B **300**, 29 (1993).
- [43] A. Wieloch et al., Phys. Lett. B. **432**, 29 (1998).
- [44] T. Lefort et al., Nucl. Phys. A. **662**, 397 (2000).
- [45] R. Nebauer et al., Nucl. Phys. A. **658**, 67 (1999).
- [46] R. Pak et al., Phys. Rev. C **54**, 1681 (1996).
- [47] T. X. Liu et al., submitted (2004).
- [48] R. J. Charity, Private Communication (2004).
- [49] D. H. E. Gross, Rep. Prog. Phys. **53**, 605 (1990).
- [50] S. Albergo et al., Nuovo Cimento A **89**, 1 (1985).
- [51] J. Pochodzalla et al., Phys. Rev. Lett. **75**, 1040 (1995).